Communication

Photo-Rechargeable Zinc-Ion Capacitor using 2D Graphitic Carbon Nitride

Dr. Buddha Deka Boruah, Angus Mathieson, Bo Wen, Changshin Jo, Felix Deschler, and Michael De Volder

Nano Lett., **Just Accepted Manuscript** • DOI: 10.1021/acs.nanolett.0c01958 • Publication Date (Web): 26 Jun 2020

Just Accepted

is published by the American Chemical Society. 1155 Sixteenth Street N.W., Washington, DC 20036

Photo-Rechargeable Zinc-Ion Capacitor using 2D Graphitic Carbon Nitride

Buddha Deka Boruah[1,*], Angus Mathieson[1,2], Bo Wen[1,2], Changshin Jo[1], Felix Deschler[3], Michael De Volder[1,*]

[1] Institute for Manufacturing, Department of Engineering, University of Cambridge, Cambridge CB3 0FS, United Kingdom
[2] Cambridge Graphene Centre, University of Cambridge, Cambridge CB3 0FA, United Kingdom
[3] Walter Schottky Institut, Fakultät für Physik, Technische Universität München, Am Coulombwall 4, 85748 Garching bei München

* Corresponding authors. E-mail: bd411@cam.ac.uk
E-mail: mfld2@cam.ac.uk

Abstract

Off-grid energy storage devices are becoming increasingly important to power distributed applications such as internet of things and smart city ubiquitous sensor systems. To date, this has been achieved by combining an energy storage device e.g. battery or capacitor with an energy harvester e.g. solar cell. However, this approach inherently increases device footprint, and the output voltages of energy harvesters often do not match those required by energy storage device. We introduce the first photo-rechargeable zinc-ion capacitors, where graphitic carbon nitride is used as at the same time as the capacitor electrode and light harvesting material. This approach allows for light to recharge the capacitor directly, and can be operated in a continuous light powered mode. These capacitors show a photo-rechargeable specific capacitance of ~ 11377 mF g^{-1}, a photo-charging voltage response of ~ 850 mV and a cyclability with ~ 90% capacitance retention over 1000 cycles.

KEYWORDS: Hybrid zinc-ion capacitor, photo-rechargeable, off-grid energy, graphitic carbon nitride.

The development of off-grid energy storage devices is becoming increasingly important to fulfil the requirements of continuous data processing and transmission for Internet of things (IoT), smart cities and autonomous integrated devices.[1-3] Previously, the design of energy supplies for standalone devices involved the extrinsic combination of a separate energy harvesting component (e.g. photovoltaic solar cells) and a rechargeable energy storage component (e.g. batteries, supercapacitors, hybrid capacitors). For instance, Um *et al.* reported a photo-rechargeable solid-state lithium-ion battery (LIB) integrated with Si solar cells,[4] Du *et. al.* fabricated a flexible solid-state graphene-based supercapacitor and perovskite solar cell integrated system,[5] Li *et al.* also recently reported a photo-rechargeable lithium-ion capacitor driven by a perovskite solar cell.[6] However, the external integration of solar cells with rechargeable devices results in an increase of the overall device footprint, increases ohmic transport losses, and requires additional external electronics to match the output of the solar cell to the energy storage device.[7,8] Direct printing of both solar cells and rechargeable devices in the same housing by layer-by-layer device fabrication approach have been applied to overcome some issues of reducing packaging volume to increase volumetric energy storage performance and reduce in ohmic transport losses.[9-11] For instance, Liu's group reported a fiber-shaped supercapacitor integrated with a dye-sensitized solar cell sharing an electrode.[12] Liang *et al.* also reported shared electrode based supercapacitor and perovskite solar cell systems.[13,14] However, this approach usually increases the overall device complexity and fabrication cost. Photoelectrodes based on the physical combination of photovoltaic and hybrid energy storage materials can be realized in a single device architectures.[15-17] However, such devices offer limited photo-charging performance due to issues such as inefficient transportation of photogenerated charge carriers from photovoltaic materials to energy storage materials because of energy levels mismatch at the interface between the two materials, inefficient photon absorption in the photovoltaic active material due to the blocking of light by the energy storage

material, phase separation of the photovoltaic and energy storage materials during fabrication and an increase in resistance due to interfacial effects between the two components. Therefore, it is desirable to explore new materials that combine photovoltaic and energy storage capabilities simultaneously, as proposed recently for LIBs using perovskite based electrodes.[8,18-20]

Recently, zinc-ion capacitor (ZIC) has been proposed as a promising energy storage technology, capable of balancing energy and power density favourably along with excellent safety and cycling life.[21-24] Here, we present the first photo-rechargeable ZIC (Photo-ZIC) using 2D graphitic carbon nitride (g-C_3N_4) photo-cathode for the simultaneous harvesting of solar energy and charge storage. **Figure 1a** depicts the proposed photo-ZIC device architecture schematically. The 2D g-C_3N_4 shown in **Figure 1b** is used as a photo-active cathode material because of its unique combination of a band gap in the visible spectrum (~ 2.7 eV see further) and high surface area desirable for ZIC cathodes (ion adsorption). Our 2D g-C_3N_4 was characterised by X-ray diffraction (XRD), Fourier-transform infrared spectroscopy (FTIR), Brunauer-Emmett-Teller (BET) and thermographic analysis (TGA) which are provided in **Figure S1-S4**. The light induced changes in electrochemical properties of g-C_3N_4 electrodes was first characterized in a beaker cell using three-electrode cyclic voltammetry (CV) measurements both in the dark and under illumination ($\lambda \sim 420$ nm, intensity ~ 50 $mWcm^{-2}$) using the setup shown in **Figure 1c**. In order to facilitate the transport of photo-excited electrons, a favourable energy band alignment is achieved by mixing g-C_3N_4 (93 wt%) with reduced graphene oxide (rGO, 2wt%) as described in the experimental section. The rGO acts as a conductive additive and selective electron transport layer in the photo-cathode – allowing the flow of photo-excited electrons to the anode through the external circuit. **Figure S5** shows SEM, XRD and Raman characterisations of the rGO used in our devices, and top-view and

cross-section SEM images of the photo-cathodes are provided in (**Figure S6a** and **b** respectively).

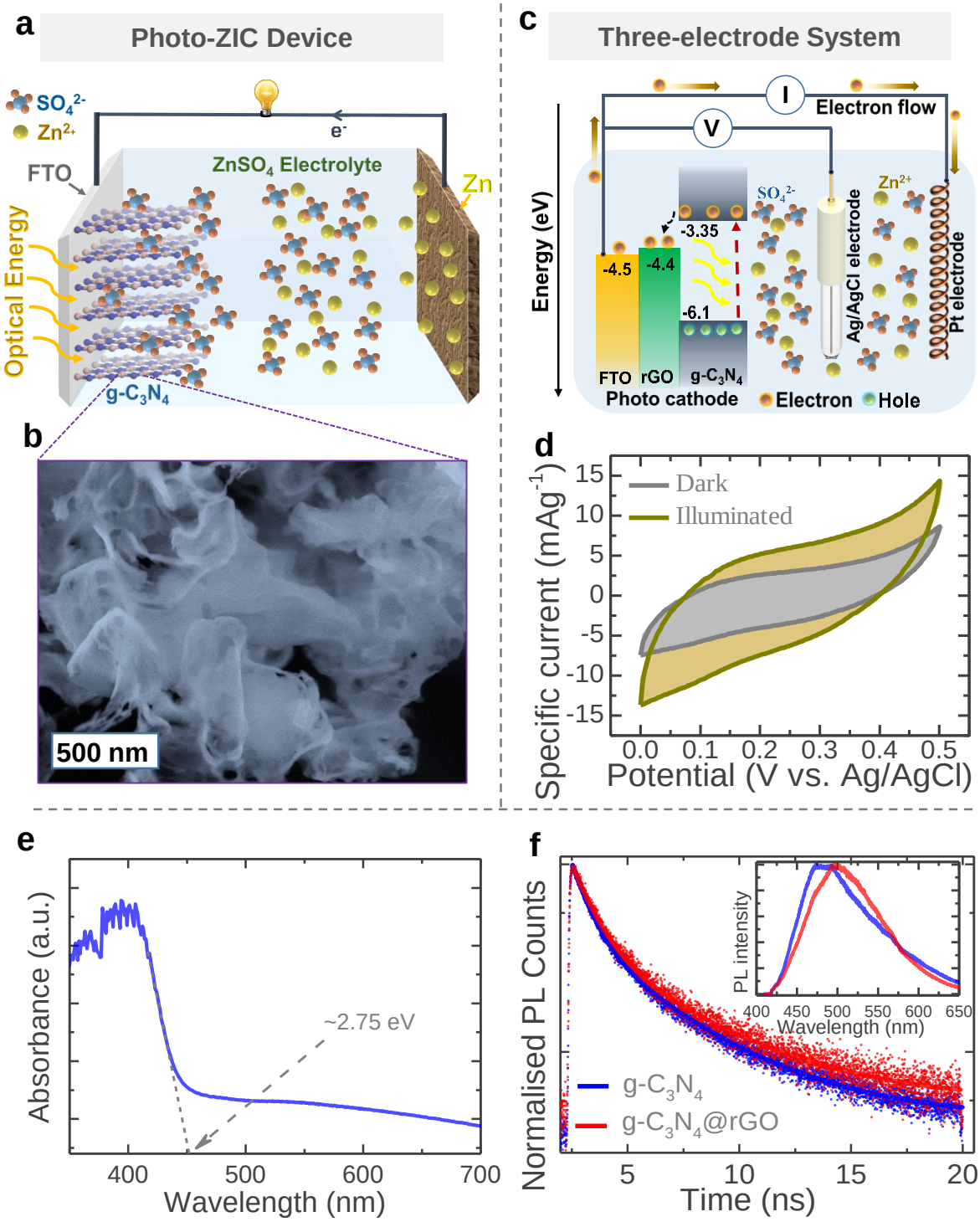

Figure 1. *(a,b) Schematic illustration of 2D g-C_3N_4 cathode and Zn anode based photo-ZIC and SEM image of 2D g-C_3N_4. (c) Schematic representation of a three-electrode experiment of*

g-C_3N_4@rGO/FTO electrodes. (d) CV profiles (10 mVs^{-1}) in dark and illuminated conditions (λ ~ 420 nm, intensity ~ 50 $mWcm^{-2}$). (e) Optical absorption spectrum of g-C_3N_4. (f) Time resolved PL signal of g-C_3N_4 (blue) and g-C_3N_4@rGO (red) samples (log scale on y-axis). Lines are exponential fits to the data. (Inset) normalised steady-state PL emission spectra of g-C_3N_4 (blue) and g-C_3N_4@rGO (red).

For the three-electrode experiments, the electrodes are drop-casted on fluorine-doped tin oxide (FTO)-coated glass substrates (see **Figure 1c**). **Figure 1d** shows the CV responses (at a scan rate of 10 mVs^{-1}) of the g-C_3N_4@rGO/FTO in the dark and under illumination. The area enclosed by the CV curve increases under illumination relative to the dark scan from which we calculate a capacitance enhancement of ~ 82% ($= \frac{C_{light}-C_{dark}}{C_{dark}} \times 100\%$; with C_{light} and C_{dark} the specific capacitances in illuminated and dark conditions at same scan rate). Similarly, CV scans at 50 mVs^{-1}, 70 mVs^{-1} and 100 mVs^{-1} in dark and illuminated conditions show an enhancement of ~ 58%, ~ 47% and ~ 43% (**Figure S7a-c**). The increase in specific capacitance of g-C_3N_4@rGO/FTO under illumination is attributed to the increased charge carrier density from the photo-excited electrons and holes when illuminated with a wavelength λ ~ 420 nm (~ 2.95 eV), which is higher energy than the band gap of g-C_3N_4 (~ 2.75 eV from the UV-Vis spectrum in **Figure 1e**). We suggest that the photogenerated electrons transfer from g-C_3N_4 to FTO through the rGO, whereas photogenerated holes participate in anions adsorption on the electrode surface to enhance the overall specific capacitance under illumination (see further). Control experiments using only rGO or activated carbon electrodes without g-C_3N_4 do not show a photo response as shown in **Figures S8**.

Photoluminescence (PL) spectra of pristine g-C_3N_4 and g-C_3N_4@rGO suggest the transport of photogenerated electrons from g-C_3N_4 to rGO. **Figure 1f** (inset) compares the PL emission of pristine g-C_3N_4 (blue) and g-C_3N_4@rGO (red), with both samples demonstrating the expected

broad PL emissions from the multiple photoactive energy levels of the material.[25] An apparent increase on the red side of the spectrum is observed upon the addition of rGO, indicating the introduction of new photoactive sub-gap energy levels from the rGO and hence, resulting in pathways for lower-energy recombination and PL emission. **Figure 1f** shows the photo-excited charge carrier lifetimes of the pristine g-C_3N_4 (blue) and g-C_3N_4@rGO (red). Average lifetimes are extracted from bi-exponential fitting of the PL decay and values of 1.76 ns ± 0.02 and 1.95 ns ± 0.02 are calculated for the pristine g-C_3N_4 and g-C_3N_4@rGO samples respectively, corresponding to a ~11% increase in charge carrier lifetime after adding rGO. Due to the favourable energy pathway (as discussed earlier in **Figure 1c**), the photo-excited electrons preferentially transfer from g-C_3N_4 to rGO thus increasing the average time between excitation and recombination/emission.

The results presented this far were obtained in beaker cells using platinum wire (Pt) counter electrodes, in what follows, g-C_3N_4@rGO/FTO cathodes are paired with a metallic zinc (Zn) anodes to form Photo-ZICs. Metal anodes and in particular Li metal anodes in LIBs, often suffer from dendrite formation, which can cause short-circuits and subsequent ignition of the electrolyte which is a major safety risk.[26] Here however, we are using a non-flammable aqueous electrolyte, and some publications seem to indicate that Zn anodes are fairly stable over extended cycle show superior capacitance stability over more than 10000 cycles.[21-24] Post-mortem SEM imaging of our Zn anodes after 1000 cycles did not show any signs of dendrite formation (see further). The electrodes are mounted in CR2450 coin cells in which we machined holes and mounted ~ 8 mm diameter optical glass to allow for illumination (see experimental section and **Figure S9a**). CV scans of the photo-ZICs were evaluated in dark and illuminated conditions (λ ~ 420 nm, intensity ~ 50 $mWcm^{-2}$) in 2M zinc sulfate ($ZnSO_4$) aqueous electrolyte.

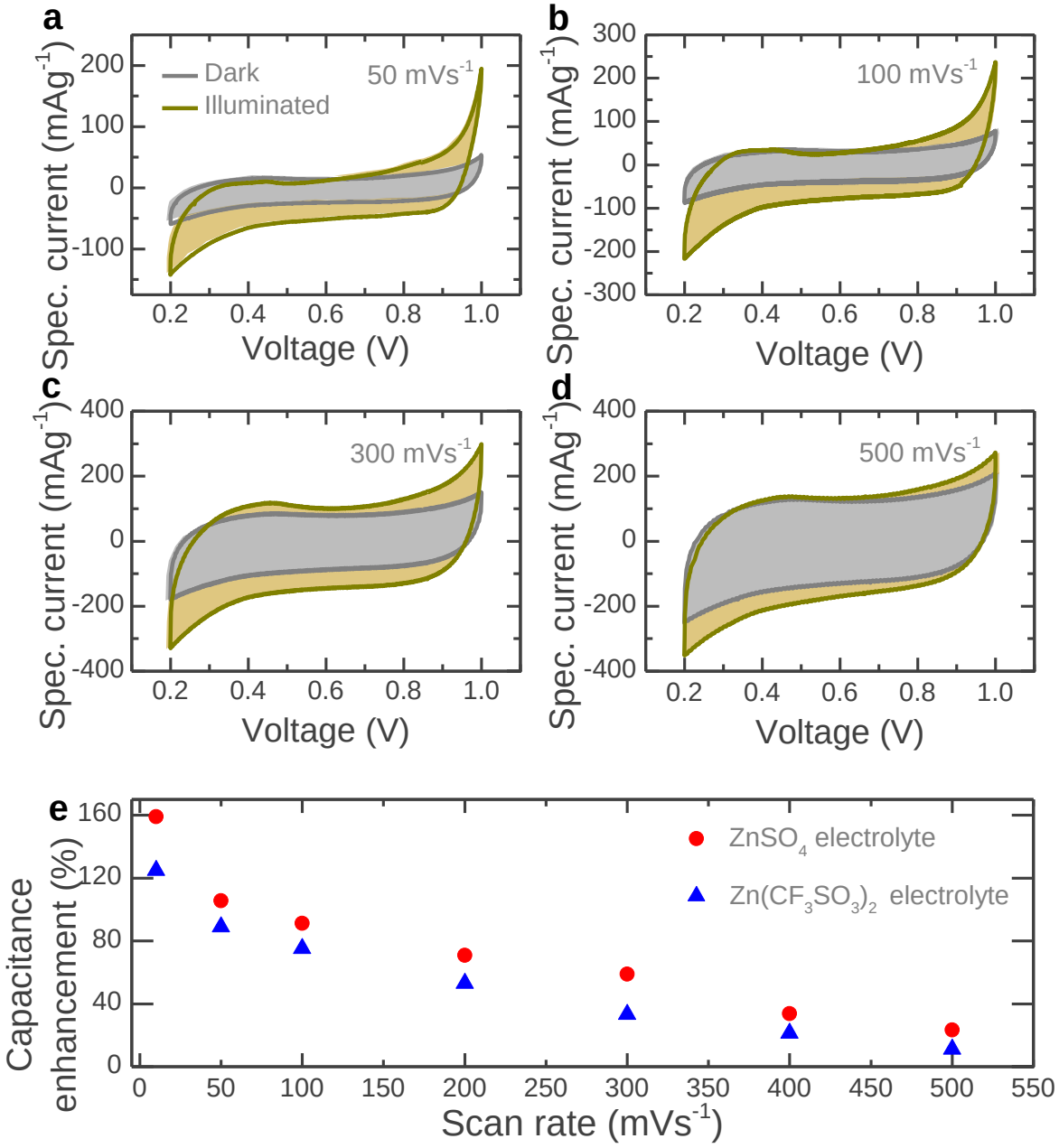

Figure 2. *CV comparison of the Photo-ZIC at different scan rates of (a) 50 mVs^{-1}, (b) 100 mVs^{-1}, (c) 300 mVs^{-1} and (d) 500 mVs^{-1}in dark and illuminated (λ ~ 420 nm, intensity ~ 50 mWcm^{-2}). (e) Capacitance enhancement with respect to scan rate of the Photo-ZIC in $ZnSO_4$ and $Zn(CF_3SO_3)_2$ aqueous electrolytes under light illumination (λ ~ 420 nm, intensity ~ 50 mWcm^{-2}).*

Figure 2a-d show the respective CV profiles at different scan rates of 50 mVs^{-1}, 100 mVs^{-1}, 300 mVs^{-1} and 500 mVs^{-1} (**Figure S9b**, CV responses in dark). Enhancements of up to 160%

are achieved at slow scan rates (10 mVs^{-1}), and even at fast scan rates (500 mVs^{-1}) enhancements of 23.43% are observed despite the relative limited time for light charging at fast scan rates. The CV response under illumination is slightly distorted under illumination, especially around 0.2 and 1 V (see **Figure 2a-d**), which may be due to photocatalytic decomposition of the aqueous electrolyte. This effect is strongly reduced when using 1M zinc trifluoromethanesulfonate ($Zn(CF_3SO_3)_2$) as an electrolyte (see **Figure S10**). **Figure 2e** shows that both electrolytes offer a comparable performance, which again suggests that g-C_3N_4 is driving the light charging rather than side reactions.

The photo-charging principle of the Photo-ZICs can be explained from the energy level diagram (**Figure S11a**). As outlined schematically in **Figure 1c**, the photogenerated electrons transport from g-C_3N_4 to FTO through rGO and finally accumulate on the Zn anode through the external circuit. The photogenerated free holes attract anions (e.g. SO_4^{2-}) towards the g-C_3N_4@rGO cathode for adsorption on the surface, while the accumulated photogenerated electrons on Zn anode may help the deposition of cations (Zn^{2+}) from the electrolyte (e.g. 2 M $ZnSO_4$). Overall, this process results in the photo-charging of Photo-ZICs under illumination. The photo-charging process of the Photo-ZICs can be further confirmed from the light-dependent chronoamperometry measurement *i.e.* current versus time plot at zero applied voltage as shown in **Figure S11b.** It is observed that the current response ($\Delta I = I_{light} - I_{dark}$) of the Photo-ZIC increases from 0 µA to ~ 68 µA (~ 136 μAcm^{-2}) under light illumination (λ ~ 420 nm, intensity ~ 50 $mWcm^{-2}$) and returns to 0 µA in dark conditions. The increase in the current response of the Photo-ZIC under light illumination is due to the transportation of the photogenerated electrons from cathode to anode through the external circuit for photo-charging the Photo-ZIC at zero applied voltage. Moreover, to elucidate the contribution of the different materials, we measured CV responses of rGO/FTO//Zn and activated carbon/FTO//Zn based ZICs in dark and illuminated conditions (**Figure S12a,b**). As anticipated from the energy band

diagram (**Figure 1c**), these do not show any photo-charging responses. In addition, we have replaced rGO by a standard SuperP conductive additive (same wt%), however, these electrodes showed very poor photo-charging as shown in **Figure S12c**. We think this is possibly due to a combination of higher light absorption and poor interface between the g-C_3N_4 and SuperP particles, and energy levels mismatch at the interface between the two materials.

The influence of the light wavelength on the photo-charging process is shown in **Figure 3a** (CV responses in **Figure S13**). As expected, negligible capacitance enhancements is observed at 528 nm, 470 nm and 455 nm excitation because the corresponding excitation energies of ~ 2.34 eV, ~ 2.63 eV and ~ 2.72 eV, respectively are lower than the optical band gap of g-C_3N_4 (~2.75 eV). However, a significant capacitance enhancement of ~ 71% is recorded when exposed to 420 nm (~2.95 eV) due to the photogeneration of electrons and holes initiating the aforementioned photo-charge mechanism. We also confirmed that the absorption spectra of the Photo-ZICs does not change with the state of charge by mounting an optical ZIC cell in a UV-Vis with integrating sphere and analysing the reflection spectra in operando while cycling (**Figure S14**).

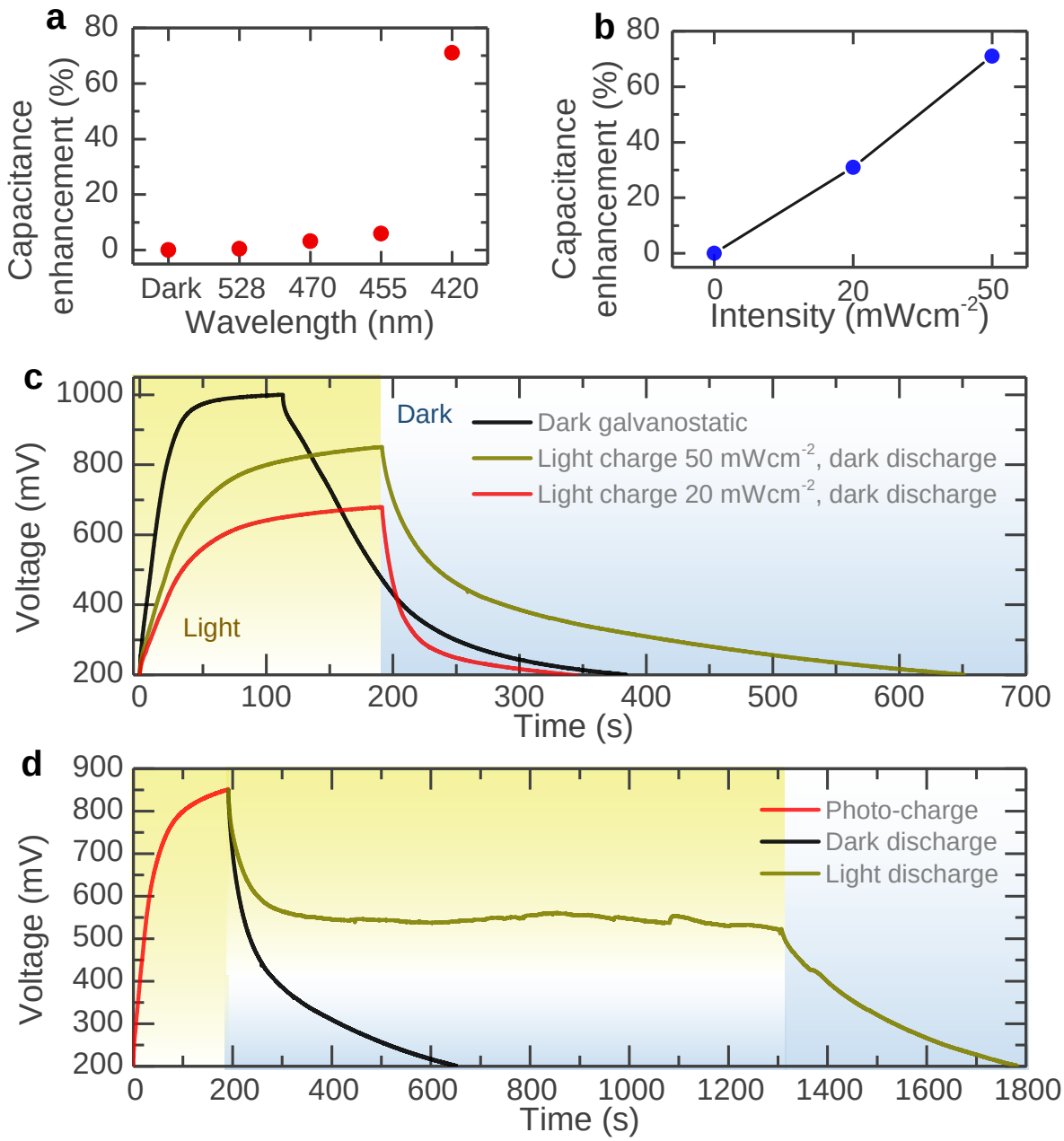

Figure 3. *(a) Wavelength dependence capacitance enhancement of the Photo-ZIC device. Scan rate = 200 mVs^{-1}. (b) Intensity dependence capacitance enhancement of the Photo-ZIC at λ ~ 420 nm. (c) Conventional charge-discharge at 10 mAg^{-1} and photo-charged (λ ~ 420 nm at intensity ~ 20 mWcm^{-2} and intensity ~ 50 mWcm^{-2}) and discharged at 10 mAg^{-1} in dark of the Photo-ZIC. (d) Photo-charged (λ ~ 420 nm, intensity ~ 50 mWcm^{-2}, red) and discharged at 10 mAg^{-1} in dark (black) and illuminated (dark yellow) conditions.*

Figure 3b shows the capacitance increases from ~ 31% to ~ 71% when increasing the light intensity from 20 $mWcm^{-2}$ to 50 $mWcm^{-2}$ (**Figure S15**, CV profiles). The increased intensity results in an increased rate of photocharge carrier generation thereby increasing the number of charge carriers available to contribute to the photo-charging mechanism and thus the observed capacitance enhancement. Next, we compare charging Photo-ZICs galvanostatically (current of 10 mAg^{-1} and cut off voltage 1000 mV) with light charging using intensities of 20 $mWcm^{-2}$ and 50 $mWcm^{-2}$. The latter converged to output voltages of approximately ~ 680 mV and ~ 850 mV, respectively after 200 s (see **Figure 3c).** The differences between the output voltage using galvanostatic and light charging is in part due to limitations in the penetration depth of light in the electrode. In addition, we expect that increasing the light intensity enhance the photocharge carrier generation efficiency, resulting in higher charging rates at higher light intensities. Finally, we observed that prolonged light charging time at 50 $mWcm^{-2}$ resulted in output voltages up to ~ 930 mV (see further). However, by comparison, the photo-charging voltage response (~ 850 mV) of our Photo-ZICs is comparable with the best reported an integrated photo-rechargeable supercapacitors with solar cells as summarized in **Table S1**. If the electrodes are continuously exposed to light while discharging at 10 mAg^{-1}, the output voltage drops from ~ 850 mV to ~ 550 mV, but then remains constant as a balance is achieved between the photo-charging and discharge currents (see **Figure 3d**). When the light is subsequently turned off, the photo-ZIC output voltage drops as expected. Overall, this demonstrates the ability of the g-C_3N_4 Photo-ZIC to operate simultaneously as an energy storage and photovoltaic device.

Figure 4a shows photo-charge ($\lambda \sim 420$ nm, intensity ~ 50 $mWcm^{-2}$) followed by galvanostatic discharge cycles at specific currents of 5 mAg^{-1} to 50 mAg^{-1}, which are used to calculate the specific capacitances, energy densities and power densities shown in **Figure 4b**. Our photo-charged capacitances of up to 11377 mFg^{-1} are comparable with values reported for

conventional solid-state supercapacitors.[27,28] Based on the photo-charging responses of the Photo-ZIC, we calculate the photo-charged energy density and power density of the Photo-ZIC at different discharge specific currents. Photo-charged energy densities and power densities of 668 $mWhkg^{-1}$ at 1625 $mWkg^{-1}$ and 87.93 $mWhkg^{-1}$ at 16250 $mWkg^{-1}$ are found at discharge specific currents of 5 mAg^{-1} and 50 mAg^{-1}. The photo-charging conversion efficiency (η) of the Photo-ZIC is ~ 0.01% (see calculation in supporting information). This value is relatively low compared to systems using energy storage devices (battery or supercapacitor) integrated with solar cells (see **Table S1**).[10,11] Also the energy efficiency in charging and discharging is still low at this stage, but we anticipate that this can be increased by tuning the electrode composition and morphology.

The stability of the Photo-ZICs is investigated by repeated photo-charging (λ ~ 420 nm, 50 $mWcm^{-2}$ and 100 s illumination) followed by galvanostatic discharging (to 200 mV) as shown in **Figure 4c**. Repeatable photo-charging (negligible capacity loss ~ 1.4%) is observed during the cycling test for nine cycles. We measured the self-discharge rate of a photo-charged Photo-ZIC device (see **Figure S16a**), which shows a ~ 17 % voltage loss after 20 hours, this value is comparable or even lower than other supercapacitors reported in literature.[29-33] Also, the floating voltage of the devices was measured under prolonged illumination (3000 s) as shown in **Figure S16b**. To further test the long-term cycle stability of the Photo-ZIC, the cell was cycled for 500 cycles in dark conditions (**Figure S17a**), after which a low capacitance degradation of ~ 4.7% over 500 cycles is observed in the Photo-ZIC as shown in **Figure S17b**. After 500 galvanostatic cycles, we photo-charged (λ ~ 420 nm, intensity ~ 50 $mWcm^{-2}$) the Photo-ZIC and discharged at 20 mAg^{-1}, which shows a negligible loss of capacity as shown in **Figure 4d**. Similarly, we cycled a cell for 1000 CV scans at 500 mVs^{-1} under illumination (λ ~ 420 nm, intensity ~ 50 $mWcm^{-2}$) and found a capacitance loss of 6.2% after 500 cycles and 10.8% after 1000 cycles (see **Figure S18)**. Likewise, **Figure 4e** shows the AC impedance

spectra of the Photo-ZIC before and after 500 charge-discharge cycles, where the equivalent series resistance increases from 16 Ω to 21.8 Ω. In addition, no notable changes in the photo-cathode morphology are observed using post-mortem SEM analysis of the cathode after 1000 CV cycles (see **Figure S19a,b**). Similarly post-mortem SEM imaging of the Zn anode shows a slight increase in surface roughness, which is probably due to cations deposition and stripping during charge and discharge (**Figure S19c,d**). Moreover, PL spectra of g-C_3N_4@rGO/FTO cathodes before and after cycling show the same emission spectra positions centred at $\lambda \sim 470$ nm, 492 nm and 524 nm with only a subtle increase from the emission at 524 nm (**Figure S19e**). Overall, this confirms that the optical properties of the electrode are not altered significantly by long-term cycling (~ 1000 illuminated cycles) and that the optical properties are maintained.

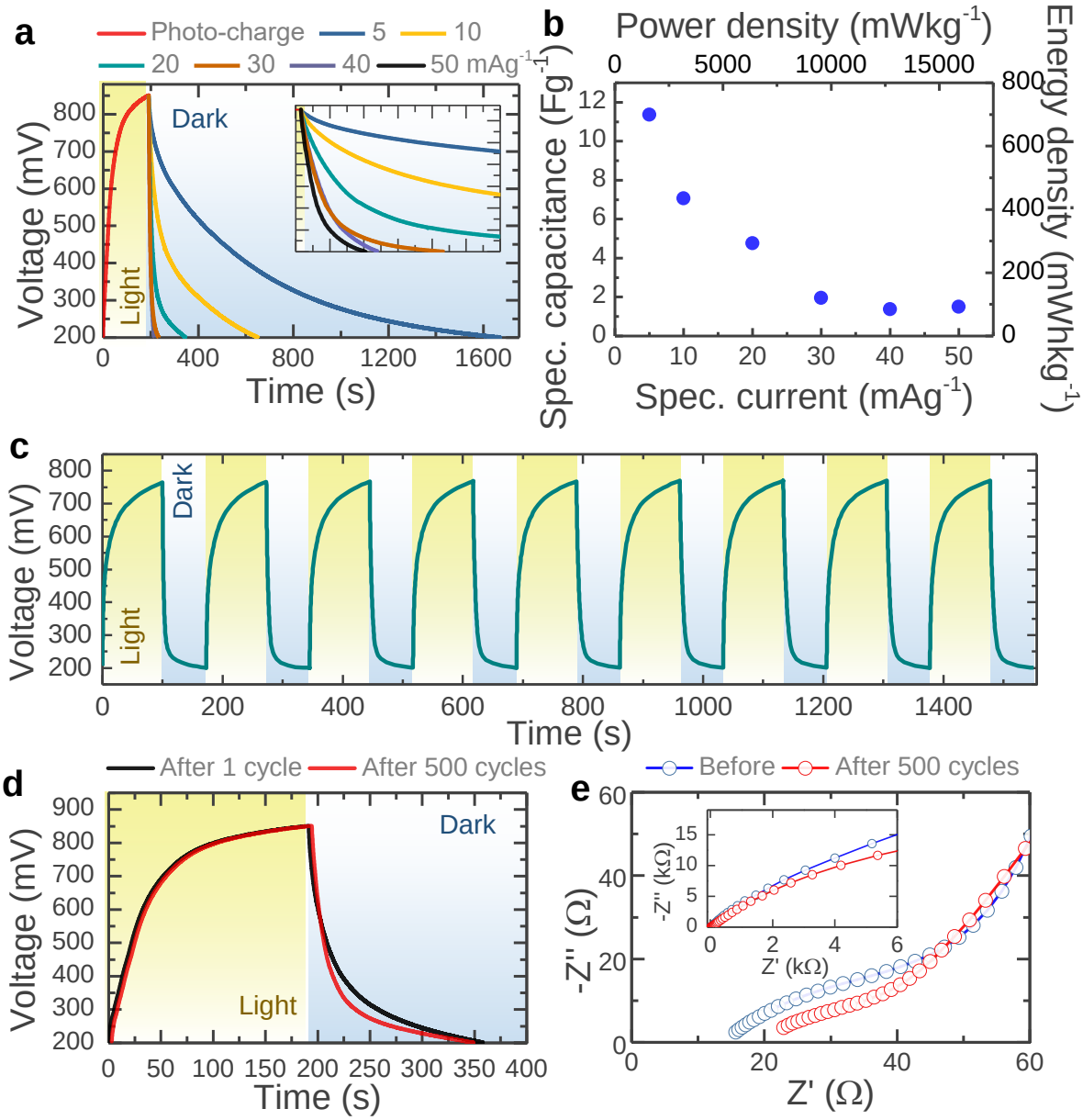

Figure 4. *(a) Photo-charge (λ ~ 420 nm, intensity ~ 50 mWcm^{-2}) and discharge cycles at different specific currents of 5 mAg^{-1}, 10 mAg^{-1}, 20 mAg^{-1}, 30 mAg^{-1}, 40 mAg^{-1} and 50 mAg^{-1}. (b) Photo-charged specific capacitance, energy density and power density plots as a function of discharge specific currents of the Photo-ZIC. (c) Cyclic photo-charge (λ ~ 420 nm, intensity ~ 50 mWcm^{-2}) and discharge cycles at a constant specific current. (d) Comparison plot of 1st photo-charging and after 500 charge-discharge cycles. (e) Nyquist plot of the Photo-ZIC before and after 500 charge-discharge cycles.*

This study demonstrates the first photo-rechargeable ZIC, which uses g-C_3N_4 as active material to achieve direct charging by light without using any external photovoltaic devices. These ZICs achieve photo-charged specific capacitances of up to 11377 mFg^{-1} and retain ~ 90% of their capacity over 1000 cycles. Because of the simple device architecture compared to alternative solutions using a combination of photovoltaics and energy storage systems, we anticipate that this technology could be of interest for powering ultra-low power compact off-grid devices, for instance in IoT applications.

Experimental Section

Chemicals. Urea, $Zn(CF_3SO_3)_2$, N-Methyl-2-pyrrolidone (NMP) and 2 M $ZnSO_4$ solution are received from Sigma-Aldrich. Graphene oxide (GO, 0.4 wt% in water) solution and activated carbon were purchased from Graphenea and Alfa Aesar. The epoxy (EVO-STIK) and polyvinylidene fluoride (PVDF, Solef 6020) binder are received from Arco Ltd and Solvay.

Synthesis of g-C_3N_4. Commercially available urea was used as a precursor of g-C_3N_4. First, 5 g urea was dried at 70 ^oC for 5 h in air, then transferred into a crucible and covered with a lid. The crucible was placed into a atmospheric pressure muffle furnace, then the furnace temperature was increased to 530 ^oC and maintained for another 3 h. During this step, stable g-C_3N_4 is formed. Thereafter the furnace was cooled down to room temperature and the yellow product was then collected and washed with deionised water and ethanol followed by vacuum filtration process. Final product was dried at 120 ^oC for 12 h in a vacuum oven.

Synthesis of rGO. GO was collected from graphene oxide solution by drying at 70 ^oC for 24 h. As obtained GO was reduced at 350 ^oC in helium gas (100 sccm, used as a carrier gas) and hydrogen gas (100 sccm) environment for 3 h using tubular CVD furnace.

Materials Characterizations. SEM images are taken using a FEI Magellan 400L with an acceleration voltage of 5 kV. XRD patterns are collected using a Bruker D8 Advance (Cu Kα

radiation). BET surface area characterization is measured using a Micromeritics 3Flex under nitrogen environment and TGA is performed using a PerkinElmer Pyris1 instrument machine in air. FTIR measurement is recorded using a PerkinElmer Frontier FT-IR Spectrometer.

Preparation of Electrodes. First, 2 mg rGO was dissolved into 2 ml NMP followed by ultra-sonication process for 5 h. Thereafter, 93 mg g-C_3N_4 was added in the same rGO solution and stirred for 12 h. Finally, the electrode solution was obtained by adding 5 mg PVDF binder followed by stirring another 5 h. 10 µl electrode solution was drop casted on FTO coated glass substrate (received from Sigma-Aldrich, surface resistivity ~7 Ωsq^{-1}) and dried overnight at 70 ^oC.

Three-Electrode Measurement. CV measurements of the rGO/FTO, activated carbon/FTO and g-C_3N_4@rGO/FTO electrodes are recorded using Ag/AgCl as a reference electrode and Pt wire as a reference electrode both in dark and illuminated conditions at different scan rates to confirm the photosensitivity of the electrodes.

Fabrication of Photo-ZIC. Photo-ZICs are assembled in air. First, g-C_3N_4@rGO/FTO photo-cathode with a double sided copper tape for electrical connectivity was fixed on the side of coin cell can having optical window (~ 8 mm) using EPOXY. The Whatman glass microfiber filters paper separator is placed on the photo-cathode, then 100 µl of electrolyte ($ZnSO_4$ or $Zn(CF_3SO_3)_2$) is added on the separator. On the top side of the separator, a Zn metal foil (Alfa Aesar, 0.25 mm thick) with a stainless steel disk spacer are placed. Finally, the optical coin cells are assembled followed by standard procedure.

Characterization of Photo-ZIC. All Photo-ZICs capacitive measurements were employed by using a Biologic VMP-3 galvanostat in air. The photo-charging performances are measured by illuminating light of wavelength of 420 nm (intensities ~ 50 $mWcm^{-2}$ and ~ 20 $mWcm^{-2}$). Open circuit voltages of the Photo-ZICs are recorded to obtain the photo-charging voltage response,

where photo-charged ZICs are discharged by applying different specific currents. Moreover, the CV responses of the Photo-ZICs are tested in dark and illuminated of different light wavelengths of 455 nm (intensity ~ 13.75 $mWcm^{-2}$), 470 nm (intensity ~ 43.75 $mWcm^{-2}$), 528 nm (intensity ~ 7.5 $mWcm^{-2}$) and 420 nm (intensity ~ 50 $mWcm^{-2}$), respectively over the working voltage range of 0.2 to 1 V. This working voltage of the Photo-ZIC is optimized to obtain a stable surface related charge storage capacitance of the g-C_3N_4 and avoid any gas evolution reaction.

Photoluminescence Spectroscopy. PL spectra were obtained using a confocal microscope setup in reflection (WITec alpha 300s). A 405 nm continuous wave (CW) laser was used as the excitation source with an incident power of 9.2 µW. The PL spectra shown represent the average of 3400 individual spectra obtained from a scanned area of 50 µm x 50 µm.

Time-Correlated Single Photon Counting (TCSPC). Charge carrier lifetimes were collected using TCSPC spectroscopy. A 50 µW PicoQuant LDH405 pulsed laser with λ = 407 nm and pulse length of 100 ps was used as an excitation source. The PL emission was collected at 90° and passed through a monochromator to select the collection wavelength (500 nm).

In-situ Optical Characterisation. The in-situ reflectance spectra of the Photo-ZIC cell were recorded at different charge and discharge states using PerkinElmer UV/Vis/NIR Spectrometer (Lamda 750) in reflection mode.

Supporting Information

The supporting information is available

XRD, FTIR, BET and TGA of g-C_3N_4 (Figure S1-S4); SEM, XRD and Raman of GO and rGO (Figure S5); SEM of photo-cathode (Figure S6); CV responses of g-C_3N_4@rGO/FTO, rGO/FTO and activated carbon/FTO electrodes (Figure S7,S8); digital photograph and CV profiles of Photo-ZIC (Figure S9); CV profiles in 1M $Zn(CF_3SO_3)_2$ electrolyte (Figure S10);

photo-charging mechanism and cyclic current response (Figure S11); CV curves of rGO/FTO//Zn, activated carbon/FTO//Zn and g-C_3N_4@SuperP/FTO//Zn based ZICs (Figure S12); CV responses at different light illuminated wavelengths (Figure S13); in operando optical characterisation (Figure S14); intensity dependence CV responses (Figure S15); performance comparative table (Table S1); self-discharge and voltage floating test (Figure S16); long-term cycling test (Figure S17); comparative CVs at different cycles (Figure S18), post-mortem SEM and PL analysis before and after cycling (Figure S19); photo-charge conversion efficiency calculation.

Acknowledgements

The authors BDB and MDV would like to acknowledge the support from the Newton International Fellowship-Royal Society (UK) grant NIF\R1\181656. MDV acknowledges support from the ERC MIGHTY - 866005. AM and BW acknowledge support from the EPSRC Graphene CDT EP/L016087/1. CJ acknowledges the Marie Skłodowska-Curie Actions MSCA-IF 796648.

References

1. Lethien, C.; Bideaum, J. L.; Brouss, T. Challenges and prospects of 3D micro-supercapacitors for powering the internet of things. *Energy Environ. Sci.* **2019**, *12*, 96-115.

2. Raj, A.; Steingart, D. Review—Power Sources for the Internet of Things. *J. Electrochem. Soc.* **2018**, *165*, B3130.

3. Zhan, Y.; Mei, Y.; Zheng, L. Materials capability and device performance in flexible electronics for the Internet of Things. *J. Mater. Chem. C* **2014**, *2*, 1220-1232.

4. Um, H. -D.; Choi, K. -H.; Hwang, I.; Kim, S. -H.; Seo, K.; Lee, S. -Y. Monolithically integrated, photo-rechargeable portable power sources based on miniaturized Si solar

cells and printed solid-state lithium-ion batteries. *Energy Environ. Sci.* **2017**, *10*, 931-940.

5. Du, P.; Hu, X.; Yi, C.; Liu, H. C.; Liu, P. Self-Powered Electronics by Integration of Flexible Solid-State Graphene-Based Supercapacitors with High Performance Perovskite Hybrid Solar Cells. *Adv. Funct. Mater.* **2015**, *25*, 2420-2427.

6. Li, C.; Cong, S.; Tian, Z.; Song, Y.; Yu, L.; Lu, C.; Shao, Y.; Li, J.; Zou, G.; Rümmeli, M. H.; Dou, S. Flexible perovskite solar cell-driven photo-rechargeable lithium-ion capacitor for self-powered wearable strain sensors. *Nano Energy* **2019**, *60,* 247-256.

7. Vlad, A.; Singh, N.; Galande, C.; Ajayan, P. M. Design Considerations for Unconventional Electrochemical Energy Storage Architectures. *Adv. Energy Mater.* **2015**, *5*, 1402115.

8. Ahmad, S.; George, C.; Beesley, D. J.; Baumberg, J. J.; Volder, M. D. Photo-Rechargeable Organo-Halide Perovskite Batteries. *Nano Lett.* **2018**, *18*, 1856-1862.

9. Zhou, F.; Ren, Z.; Zhao, Y.; Shen, X.; Wang, A.; Li, Y. Y.; Surya, C.; Chai, Y. Perovskite photovoltachromic supercapacitor with all-transparent electrodes. *ACS Nano* **2016**, *10*, 5900-5908.

10. Liu, R.; Wang, J.; Sun, T.; Wang, M.; Wu, C.; Zou, H.; Song, T.; Zhang, X.; Lee, S. T.; Wang, Z. L.; Sun, B. Silicon nanowire/polymer hybrid solar cell-supercapacitor: a self-charging power unit with a total efficiency of 10.5%. *Nano Lett.* **2017**, *17*, 4240-4247.

11. Xu, J.; Chen, Y.; Dai, L. Efficiently photo-charging lithium-ion battery by perovskite solar cell. *Nat. Commun.* **2015**, *6*, 8103.

12. Liang, J.; Zhu, G.; Wang, C.; Wang, Y.; Zhu, H.; Hu, Y.; Lv, H.; Chen, R.; Ma, L.; Chen, T.; Jin, Z. MoS2-based all-purpose fibrous electrode and self-powering energy fiber for efficient energy harvesting and storage. *Adv. Energy Mater.* **2017**, *7*, 1601208.

13. Liang, J.; Zhu, G.; Lu, Z.; Zhao, P.; Wang, C.; Ma, Y.; Xu, Z.; Wang, Y.; Hu, Y.; Ma, L.; Chen, T. Integrated perovskite solar capacitors with high energy conversion efficiency and fast photo-charging rate. *J. Mater. Chem. A* **2018**, *6*, 2047.

14. Liang, J.; Zhu, G.; Wang, C.; Zhao, P.; Wang, Y.; Hu, Y.; Ma, L.; Tie, Z.; Liu, J.; Jin, Z. An all-inorganic perovskite solar capacitor for efficient and stable spontaneous photocharging. *Nano Energy* **2018**, *52*, 239.

15. Paolella, A.; Faure, C.; Bertoni, G.; Marras, S.; Guerfi, A.; Darwiche, A.; Hovington, P.; Commarieu, B.; Wang, Z.; Prato, M.; Colombo, M.; Monaco, S.; Zhu, W.; Feng, Z.; Vijh, A.; George, C.; Demopoulos, G. P.; Armand, M.; Zaghib, K. Light-assisted delithiation of lithium iron phosphate nanocrystals towards photo-rechargeable lithium ion batteries. *Nat. Commun.* **2017**, *8*, 14643.

16. Nakhanivej, P.; Yu, X.; Park, S. K.; Kim, S.; Hong, J. Y.; Kim, H. J.; Lee, W.; Hwang, J. Y.; Yang, J. E.; Wolverton, C.; Kong, J. Revealing molecular-level surface redox sites of controllably oxidized black phosphorus nanosheets. *Nature Mater.* **2019**, *18*, 156.

17. Hou, R.; Gund, G. S.; Qi, K.; Nakhanivej, P.; Liu, H.; Li, F.; Xia, B. Y.; Park, H. S. Hybridization design of materials and devices for flexible electrochemical energy storage. *Energy Storage Mater.* **2019**, *19*, 212.

18. Lee, A.; Vörös, M.; Dose, W. M.; Niklas, J.; Poluektov, O.; Schaller, R. D.; Iddir, H.; Maroni, V. A.; Lee, E.; Ingram, B.; Curtiss, L. A. Photo-accelerated fast charging of lithium-ion batteries. *Nat. Commun.* **2019**, *10*, 4946.

19. Boruah, B. D.; Misra, A. Voltage Generation in Optically Sensitive Supercapacitor for Enhanced Performance. *ACS Appl. Energy Mater.* **2019**, *2*, 278-286.

20. Nguyen, O.; Courtin, E.; Sauvage, F.; Krins, N.; Sanchez, C.; Laberty-Robert, C. Shedding light on the light-driven lithium ion de-insertion reaction: towards the design of a photo-rechargeable battery. *J. Mater. Chem. A* **2017**, *5*, 5927-5933.

21. Zhang, P.; Li, Y.; Wang, G.; Wang, F.; Yang, S.; Zhu, F.; Zhuang, X.; Schmidt, O. G.; Feng, X. Zn-ion hybrid micro-supercapacitors with ultrahigh areal energy density and long-term durability. *Adv. Mater.* **2019**, *31*, 1806005.

22. Sun, G.; Yang, H.; Zhang, G.; Gao, J.; Jin, X.; Zhao, Y.; Jiang, L.; Qu, L. A capacity recoverable zinc-ion micro-supercapacitor. *Energy Environ. Sci.* **2018**, *11*, 3367-3374.

23. Zhang, X.; Pei, Z.; Wang, C.; Yuan, Z.; Wei, L.; Pan, Y.; Mahmood, A.; Shao, Q.; Chen, Y. Flexible Zinc-Ion Hybrid Fiber Capacitors with Ultrahigh Energy Density and Long Cycling Life for Wearable Electronics. *Small* **2019**, *15*, 1903817.

24. Wang, H.; Wang, M.; Tang, Y. A novel zinc-ion hybrid supercapacitor for long-life and low-cost energy storage applications. *Energy Storage Mater.* **2018**, *13***,** 1-7.

25. Yuan, Y.; Zhang, L.; Xing, J.; Utama, M. I. B.; Lu, X.; Du, K.; Li, Y.; Hu, X.; Wang, S.; Genç, A.; Dunin-Borkowski, R. High-yield synthesis and optical properties of g-C3N4. *Nanoscale* **2015**, *7*, 12343-12350.

26. Wang, J.; Yamada, Y.; Sodeyama, K.; Watanabe, E.; Takada, K.; Tateyama, Y.; Yamada, A. Fire-extinguishing organic electrolytes for safe batteries. *Nat. Energy* **2018**, *3*, 22.

27. Boruah, B. D.; Misra, A. A flexible ternary oxide based solid-state supercapacitor with excellent rate capability. *J. Mater. Chem. A* **2016**, *4*, 17552-17559.

28. Boruah, B. D.; Misra, A. Internal Asymmetric Tandem Supercapacitor for High Working Voltage along with Superior Rate Performance. *ACS Energy Lett.* **2017**, *2*, 1720-1728.

29. Chen, L.; Bai, H.; Huang, Z.; Li, L. Mechanism investigation and suppression of self-discharge in active electrolyte enhanced supercapacitors. *Energy Environ. Sci.* **2014**, *7*, 1750-1759.

30. Zhang, Q.; Cai, C.; Qin, J.; Wei, B. Tunable self-discharge process of carbon nanotube based supercapacitors. *Nano Energy* **2014**, *4*, 14-22.

31. Xiong, T.; Yu, Z. G.; Lee, W. S. V.; Xue, J. o-Benzenediol-Functionalized Carbon Nanosheets as Low Self-Discharge Aqueous Supercapacitors. *ChemSusChem* **2018**, *11*, 3307-3314.

32. Lahe¨a¨ar, A.; Arenillas, A.; B´eguin, F. Change of self-discharge mechanism as a fast tool for estimating long-term stability of ionic liquid based supercapacitors. *J. Power Sources* **2018**, *396*, 220-229.

33. Xia, M.; Nie, J.; Zhang, Z.; Lu, X.; Wang, Z. L. Suppressing self-discharge of supercapacitors via electrorheological effect of liquid crystals. *Nano Energy* **2018**, *47*, 43-50.

TOC graphic

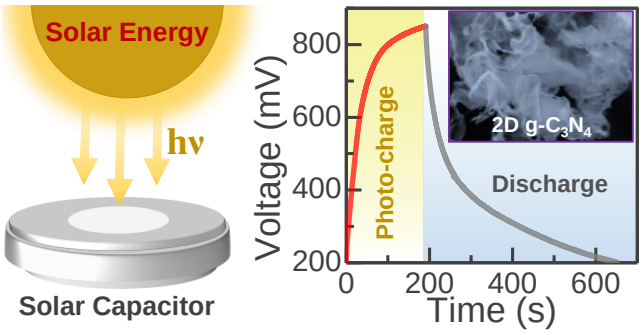
Solar Energy
hν
Solar Capacitor
Voltage (mV)
800
600
400
200
0
200
400
600
Time (s)
Photo-charge
Discharge
2D g-C3N4